

1 Band alignment of two-dimensional transition metal dichalcogenides:
2 application in tunnel field effect transistors

3
4 Cheng Gong,¹ Hengji Zhang,² Weihua Wang,¹ Luigi Colombo,³ Robert M. Wallace,^{1,2}
5 and Kyeongjae Cho^{1,2,*}

6
7 ¹Department of Materials Science and Engineering, The University of Texas at Dallas, Richardson,
8 TX 75080, USA

9 ²Department of Physics, The University of Texas at Dallas, Richardson, TX 75080, USA

10 ³Texas Instruments, Dallas, Texas 75243, USA

11

12

13 Tunnel field effect transistors (TFETs) based on vertical stacking of two dimensional materials are
14 of interest for low-power logic devices. The monolayer transition metal dichalcogenides (TMDs)
15 with sizable band gaps show promise in building p-n junctions (couples) for TFET applications.
16 Band alignment information is essential for realizing broken gap junctions with excellent electron
17 tunneling efficiencies. Promising couples composed of monolayer TMDs are suggested to be VI
18 B-MeX₂ (Me= W, Mo; X= Te, Se) as the *n*-type source and IVB-MeX₂ (Me = Zr, Hf; X= S, Se)
19 as the *p*-type drain by density functional theory calculations.

20

21

* Author to whom correspondence should be addressed. Electronic mail: kjcho@utdallas.edu

22 As the scaling of conventional metal-oxide-semiconductor field effect transistors (MOSFETs),
23 a number of challenges emerge including degraded carrier mobility, short channel effects, and
24 interfacial defect states which affect the operational speed, device stability, and the abrupt
25 switching negatively. The design and development of alternative electronic devices is urgently
26 needed and has been persistently pursued in recent years. The TFET is a promising device
27 candidate for future low-energy electronic systems, of which two characteristic parameters needs
28 careful consideration: on-off current ratio and subthreshold swing (SS).¹ Tunnel FETs based on
29 III-V materials have been explored with promising results.² However, a major challenge for
30 adopting these materials is the control of interfacial defects, such as dangling bonds, and the
31 resultant interface state density which impacts the SS.^{3,4}

32 In contrast, 2D materials, with their inherent surface bonding properties, provide an
33 opportunity to substantially reduce interface state densities, and thus mitigate SS degradation.
34 Tunnel FETs based on vertical stacking of graphene with atomically thin hexagonal boron nitride
35 (*h*-BN) or molybdenum disulfide (MoS₂) layers as separation barriers have been experimentally
36 demonstrated with precise sub-nanoscale structures.⁵ However, even though the switching
37 function is realized, the zero gap nature of graphene is still a limiting factor for increasing the
38 on-off ratios.

39 Band-to-band tunneling transport can be utilized to explore heterogeneous TFETs composed
40 of stacked source-drain junctions.⁶ Semiconducting 2D materials are of interest facilitating high
41 electron tunneling efficiency through a “broken-gap” band alignment while suppressing the OFF
42 current by band gap engineering of drain materials. Owing to the availability of a range of
43 electronic band gaps, many 2D TMDs can be considered as promising constituent materials for

44 TFET applications, since (1) the size of the band gap is tunable, *e.g.*, by mechanical strain⁷ or the
45 composition control in ternary compounds, (2) the Fermi level can be effectively adjusted by
46 doping,⁸ and (3) both band gap and Fermi level can be simultaneously adjusted by layer stacking.⁹

47 This work focuses on the systematic density functional theory (DFT) calculation of
48 individual isolated 2D TMDs. Considering the large family of TMDs, with an even larger number
49 of possible TMD stacked *p-n* junctions (“couples”), *ab initio* calculations of all TMD couples is a
50 burdensome task. Moreover, the non-trivial lattice mismatches among most TMDs provide a
51 formidable challenge for DFT. Therefore, the study of individual isolated 2D TMDs is the first
52 important step for finding clues on selecting couples suitable for TFETs. Such information will
53 also aid in providing focus to the growth of high quality 2D TMD materials, essential for accurate
54 device studies. In particular, the information about the universal band alignment of TMDs with
55 respect to the vacuum level is of practical significance.

56 We examine, by DFT calculations, the electronic properties of 24 types of 2D TMDs
57 consisting of the combinations between IVB-VIB metals (IVB: Ti, Zr and Hf; VB: V, Nb, and Ta;
58 and VIB: Mo and W) and chalcogen species (S, Se, and Te), and find that their electronic
59 properties vary dramatically. Semiconductors are found in all VIB- and some IVB-TMDs, with
60 VIB-TMDs work functions in the range of 4 to 5 eV and IVB-TMDs work functions at about 6 eV.
61 The large work function difference between VIB- and IVB-TMDs provides a way of forming
62 steep junctions with broken-gap band alignment. All of the calculated 2D VB-TMDs display
63 metallic character which will not be discussed in this Letter.

64 The calculations are performed by VASP¹⁰ with projector-augmented wave (PAW)¹¹
65 pseudopotential with both generalized gradient approximation (GGA) of Perdew-Burke-Ernzerhof

66 (PBE)¹² functional and local density approximation (LDA)¹³ to describe the exchange-correlation.
67 Spin polarization is applied for both ionic and electronic relaxation, and spin-orbit coupling (SOC)
68 is switched on for band structure calculations. In the first step, all the studied bulk TMDs are
69 relaxed based on both *2H*- and *1T*-crystal structures, with the remnant force on each atom below
70 0.01 eV/Å as the stopping criterion. Based on the optimized bulk lattice constants, monolayer
71 structures are set with a vacuum region of 17 Å normal to the surface and further relaxed with the
72 fixed unit cell shape and size. The Monkhorst-Pack k-point sampling in Brillouin zone (BZ) is
73 Γ -centered with $8\times 8\times 1$ and $40\times 40\times 1$ meshes in ionic and electronic optimization, respectively.
74 The energy cutoff is chosen at 400 eV, and the electronic optimization stops when the total
75 energies of neighboring optimization loops differ below 10^{-4} eV.

76 Reliable band alignment information of semiconductors is based on the accurate prediction of
77 two quantities: the size of band gap and the absolute energy of the Fermi level. There is a recent
78 debate about the electronic band gap of monolayer MoS₂. The value of 1.88 eV obtained by
79 photoluminescence (PL) measurements¹⁴ is in question and thought to be an excitonic gap,^{15, 16}
80 rather than a transport gap. Recent calculations incorporating the GW approximation¹⁷ collectively
81 claim a much larger quasiparticle gap of about 2.8 eV with a strong exciton binding energy of
82 about 1.0 eV, resulting in an excitonic gap of about 1.8 eV. Experimental verification of the 2.8 eV
83 transport gap has not yet been demonstrated. In addition, the calculated electron affinity of
84 monolayer MoS₂ by PBE is 4.27 eV, in this work and others.^{18, 19} However, the experimentally
85 reported electron affinity in bulk MoS₂ crystals is about 4.0 eV,²⁰ and it is known that an enlarged
86 band gap with decreased electron affinity is expected to be found in MoS₂ of decreased number of
87 layers.^{18, 21} Consequently, employing a GW correction in the calculation is necessary for gaining

88 absolute energies of band edges.

89 We carry out “single-shot G_0W_0 ” on the optimized MoS_2 structures by PBE with $12 \times 12 \times 1$
90 k-point sampling in the irreducible BZ, and a 3.0 eV quasiparticle energy gap is obtained,
91 verifying the substantially larger band gap. Converged calculation of the absolute
92 quasiparticle band edge energies requires at least ~ 1000 conduction bands included in G_0W_0
93 calculation, reported recently by Liang *et al.*¹⁹ The GW correction of the conduction band
94 minimum (CBM) and valence band maximum (VBM) was claimed to obey the
95 band-gap-center approximation, which means that there is about the same amount of shift in
96 inverse directions of both band edges relative to the same band-gap-center. According to the
97 report in Ref. 19, the gap opening by the GW correction is $\sim 50\%$ for monolayers of Mo and
98 W TMDs. Here, we do not extend the costly GW calculations to all the studied systems, but
99 include a GW correction of 50% gap opening with the band gap center (*i.e.*, Fermi level)
100 unchanged. The minor difference between gap sizes and edge energies of our results and Liang *et*
101 *al.*’s results is mainly because spin-orbit coupling (SOC) is included in our study. Based on the
102 universal band alignments of all the studied semiconducting 2D TMDs, promising material
103 couples for TFETs are suggested.

104 The total energy calculations of the optimized monolayer TMDs based on both PBE and
105 LDA show that all VIB-TMDs favor a trigonal prismatic coordination, whereas IVB-TMDs favor
106 an octahedral coordination as summarized in Table I. For convenience, the trigonal prismatic
107 coordination in monolayer is denoted as “ H ” (as opposed to the bulk terminology “ $2H$ ”), and the
108 octahedral coordination in monolayer as “ T ” (as opposed to the bulk terminology “ $1T$ ”). The
109 preferred coordination can be understood based on the electronic configuration of TM atoms and

110 the crystal field splitting. For VIB-TM atoms, the six outermost valence electrons can bond to six
111 chalcogen atoms through the trigonal prismatic coordination. As shown in Fig. 1, the effect on the
112 metal d -levels of a trigonal prismatic ligand field is splitting off of the d_z^2 subband at lower
113 energy.²² VIB-TM atoms have two electrons for filling the subband and stabilize the trigonal
114 prismatic coordination, but IVB-TM atoms do not have the two electrons to fill the d_z^2 subband so
115 that an octahedral coordination is preferred.

116 The band gaps calculated by PBE-SOC and corrected by GW based on the band-gap-center
117 approximation are plotted in Fig. 2. For the H -monolayer VIB-TMDs, as the atomic indices of
118 chalcogen species increase from S to Te, the valence band edge undergoes a conspicuous energy
119 increase, associated with a relatively smaller energy increase of conduction band edge, resulting in
120 a decreasing energy gap. As the atomic indices of chalcogen atoms increase, the larger atomic
121 radius and decreased reactivity induce weakened inter-atomic interaction strength and a larger
122 lattice constant. Thus, a smaller band gap is produced. For the same chalcogen species, Mo is
123 more reactive than W because of the intrinsic higher reactivity of $3d$ -electrons than $4d$ -electrons.
124 Hence, the overall energy levels of Mo-dichalcogenides are lower than that of W-dichalcogenides.

125 In contrast, IVB-TM atoms have one less pair of valence electrons. As a result, IVB-TMDs
126 are also semiconducting with a deeper band with respect to VIB-TMDs. Hence, the work
127 functions of IVB-TMDs are larger compared with those of VIB-TMDs. The intralayer bonding in
128 IVB-TMDs is more ionic and weaker, exhibiting generally smaller band gaps. The size of the gap
129 is strongly dependent on the TM and chalcogen species. The smaller band gaps are associated with
130 higher atomic indices of constituent chalcogen atoms, producing negative gaps in HfTe_2 and ZrTe_2 ,
131 which are predicted to be unsuitable for TFET applications. This trend is due to the decreasing

132 electron negativity of the higher-indexed chalcogen species. Semiconducting IVB-TMDs with
133 non-trivial band gaps are found in ZrS_2 , $ZrSe_2$, HfS_2 and $HfSe_2$.

134 The presence of finite band gaps but distinctive positions of band edges of VIB- and
135 IVB-TMDs imply the potential combination of these two groups of TMDs for TFET applications.
136 As indicated by results of Fig. 2, electrons at the valence band edges of WTe_2 and $MoTe_2$ would
137 be able to tunnel into the conduction bands of ZrS_2 , $ZrSe_2$, HfS_2 and $HfSe_2$ with ease. While
138 replacing Te species by Se in VIB-TMDs, the efficiency for electron injection from VIB-TMDs to
139 IVB-TMDs decreases due to the lower valence band edges of VIB-selenides. The VBMs of MoS_2
140 and WS_2 are even lower than the CBMs of IVB-TMDs, which is detrimental for “broken-gap”
141 alignment formation and not promising for TFET applications. Considering the relative energy
142 level shift²³ for TMDs in direct contact or in contact with dielectric media, the final band
143 alignment in such systems needs further examination. The calculation herein provides useful
144 guidance for selecting the TMD material couples for TFETs.

145 It is interesting to note the intrinsic scattering in the suggested TFETs integrating VIB-TMDs
146 as the *n*-type source and IVB-TMDs as the *p*-type drain. As shown in Fig. 3, *H*-monolayer VI
147 B-TMDs have direct band gaps at K point, whereas indirect gaps are formed between Γ and M
148 points for *T*-monolayer IVB-TMDs. Correspondingly, the electron tunneling from the VBM of the
149 *H*-monolayer VIB-TMDs at the K-point to the CBM of the *T*-monolayer IVB-TMDs at the
150 M-point is anticipated to experience inelastic scattering. Engineering the position of band edges in
151 reciprocal space is a feasible scheme for addressing the issue of intervalley scattering. To this end,
152 we analyze the band edge properties of monolayer VIB- and IVB-TMDs. Insights on how strain
153 affects the band properties of monolayer TMDs are obtained.

154 For *H*-monolayer VIB-TMDs, we choose to study MoS₂ as a representative for a convenient
155 comparison with other published data. As shown in Fig. 3(a), the bonding states at $\Gamma(V)$ and $K(V)$
156 are mainly composed of out-of-plane d_z^2 -orbitals and in-plane $d_{(x^2-y^2)}+d_{xy}$ orbitals, respectively.
157 Therefore, the in-plane tensile strain weakens the inter-atomic d_z^2 - d_z^2 bonding more than the
158 $d_{(x^2-y^2)}$ - $d_{(x^2-y^2)}$ and d_{xy} - d_{xy} bondings. The resulting energy level shifting up of the d_z^2 - d_z^2 bonding
159 state $\Gamma(V)$ is more than that of the bonding state $K(V)$. For the anti-bonding states, $K(C)$ is
160 composed of a higher weight of out-of-plane oriented orbitals than $\Gamma K(C)$. Hence, the in-plane
161 tensile strain shifts the energy position of $K(C)$ downward in a larger amount compared with that
162 of $\Gamma K(C)$. The tensile strain is inferred to produce a reduced indirect band gap between $\Gamma(V)$ and
163 $K(C)$, whereas the compressive strain is expected to produce an increased indirect band gap
164 between $K(V)$ and $\Gamma K(C)$. These findings agree well with the reported strain-induced band gap
165 evolution by first-principle simulations.^{7, 9, 24, 25}

166 For *T*-monolayer IVB-TMDs, ZrS₂ is studied as a representative system. The intrinsic band
167 gap is indirect between Γ as VBM and M as CBM. Interestingly, as shown in Fig. 3(b), among
168 $\Gamma(C)$, $\Gamma(V)$, $M(C)$ and $M(V)$, only $M(C)$ has a significant portion of out-of-plane oriented orbitals
169 $Zr-dz^2$ and $S-pz$. Hence, strain is expected to affect the position of $M(C)$ more than that of others.
170 We apply 5% tensile and compressive strains, and find that $M(C)$ shifts up with tensile strain and
171 shifts down with compressive strain, but $\Gamma(C)$, $\Gamma(V)$ and $M(V)$ do not change much. Upon the
172 application of larger than 5% tensile strain, the CBM begins to transit from M to Γ . Tensile strains
173 are indicated to be able to modify both the VBM of 2D VIB-TMDs and the CBM of 2D
174 IVB-TMDs to Γ point, potentially eliminating the inelastic scattering in tunneling process.

175 In summary, by systematic DFT calculations, we found semiconductors in 2D form of both

176 VIB- and IVB-TMDs. The two groups of semiconductors have distinct work functions, exhibiting
177 the potential of being stacked for TFET applications. With more accurate prediction of the
178 quasiparticle energy gap by GW corrections, promising 2D TMDs couples still exist. We suggest
179 the layer coupling using VIB-MeX₂ (Me= W and Mo; X= Te and Se) as the *n*-type source and IV
180 B-MeX₂ (Me = Zr and Hf; X= S and Se) as the *p*-type drain, for vertically stacked TFET
181 applications. The two groups of semiconductors have distinct band edge characters, which
182 intrinsically incur intervalley scattering during the electron tunneling process. Strain is highlighted
183 as an effective way to modify the band edge properties of these 2D TMDs. Interface related issues
184 need to be carefully examined in realistic TFET designs and fabrication where the work functions
185 of 2D materials is inevitably modified by contact to surrounding media. In addition, the
186 conclusion about the preferential couples in this Letter is based on the stacking of monolayers.
187 Heterogeneous junctions between multilayer TMDs require further study, and the precise band
188 realignment caused by interface charge transfer and interface dipole formation when two isolated
189 monolayers couple together, will be the focus of a follow-up work. At the current stage of research,
190 the fundamental understanding of the TMD family provided here will inspire exciting ideas and
191 applications.

192

193 This work was supported by the Center for Low Energy Systems Technology (LEAST), one of six
194 centers supported by the STARnet phase of the Focus Center Research Program (FCRP), a
195 Semiconductor Research Corporation program sponsored by MARCO and DARPA. HZ is
196 partially supported by Nano-Material Technology Development Program through the National
197 Research Foundation of Korea (NRF) funded by the Ministry of Science, ICT and Future Planning
198 (2012M3A7B4049888).

199

200 ¹ A. M. Ionescu and H. Riel, *Nature* **479**, 329 (2011).
201 ² A. C. Seabaugh and Q. Zhang, *PROCEEDINGS OF THE IEEE* **98**, 2095 (2010).
202 ³ W. Wang, C. L. Hinkle, E. M. Vogel, K. Cho, and R. M. Wallace, *Microelectron. Eng.* **88**,
203 1061 (2011).
204 ⁴ C. L. Hinkle, E. M. Vogel, P. D. Ye, and R. M. Wallace, *Curr. Opin. Solid St. Mat. Sci.* **15**, 188
205 (2011).
206 ⁵ L. Britnell, R. V. Gorbachev, R. Jalil, B. D. Belle, F. Schedin, A. Mishchenko, T. Georgiou, M.
207 I. Katsnelson, L. Eaves, S. V. Morozov, *et al.*, *Science* **335**, 947 (2012).
208 ⁶ D. Jena, *PROCEEDINGS OF THE IEEE* **101**, 1585 (2013).
209 ⁷ E. Scalise, M. Houssa, G. Pourtois, V. V. Afanas'ev, and A. Stesmans, *Nano Res.* **5**, 43 (2012).
210 ⁸ H. Fang, S. Chuang, T. C. Chang, K. Takei, T. Takahashi, and A. Javey, *Nano Lett.* **12**, 3788
211 (2012).
212 ⁹ W. S. Yun, S. W. Han, S. C. Hong, I. G. Kim, and J. D. Lee, *Phys. Rev. B* **85**, 033305 (2012).
213 ¹⁰ G. Kresse and J. Furthmuller, *Comp. Mater. Sci.* **6**, 15 (1996).
214 ¹¹ P. E. Blochl, *Phys. Rev. B* **50**, 17953 (1994).
215 ¹² J. P. Perdew, K. Burke, and M. Ernzerhof, *Phys. Rev. Lett.* **77**, 3865 (1996).
216 ¹³ D. M. Ceperley and B. J. Alder, *Phys. Rev. Lett.* **45**, 566 (1980).
217 ¹⁴ K. F. Mak, C. Lee, J. Hone, J. Shan, and T. F. Heinz, *Phys. Rev. Lett.* **105**, 136805 (2010).
218 ¹⁵ T. Cheiwchanchamnangij and W. R. L. Lambrecht, *Phys. Rev. B* **85**, 205302 (2012).
219 ¹⁶ H. L. Shi, H. Pan, Y. W. Zhang, and B. I. Yakobson, *Phys. Rev. B* **87**, 155304 (2013).
220 ¹⁷ F. Aryasetiawan and O. Gunnarsson, *Rep. Prog. Phys.* **61**, 237 (1998).
221 ¹⁸ J. Kang, S. Tongay, J. Zhou, J. B. Li, and J. Q. Wu, *Appl. Phys. Lett.* **102**, 012111 (2013).
222 ¹⁹ Y. Liang, S. Huang, R. Soklaski, and L. Yang, *arXiv:1306.0620v1* (2013).
223 ²⁰ H. P. Hughes and H. I. Starnberg, *Electron Spectroscopies Applied to Low-Dimensional*
224 *Materials* (Springer, Berlin, 2000).
225 ²¹ H. Qiu, L. J. Pan, Z. N. Yao, J. J. Li, Y. Shi, and X. R. Wang, *Appl. Phys. Lett.* **100**, 123104
226 (2012).
227 ²² V. Grasso, *Electronic Structure and Electronic Transitions in Layered Materials* (D. Reidel
228 Publishing Company, Dordrecht, 1986).
229 ²³ C. Gong, G. Lee, B. Shan, E. M. Vogel, R. M. Wallace, and K. Cho, *J. Appl. Phys.* **108**,
230 123711 (2010).
231 ²⁴ H. Peelaers and C. G. Van de Walle, *Phys. Rev. B* **86**, 241401 (2012).
232 ²⁵ P. Johari and V. B. Shenoy, *ACS Nano* **6**, 5449 (2012).
233
234
235

236 TABLE I. Optimized lattice constants and total energies of monolayer TMDs, calculated by both
 237 PBE and LDA (in parenthesis). a_H and a_T are the in-plane lattice constant of trigonal prismatic and
 238 octahedral monolayer TMDs respectively. ΔE is the energy difference between trigonal prismatic
 239 and octahedral structures. Negative ΔE means the *H*-structure is more stable with lower total
 240 energy, and vice versa.

	S	Se	Te
Mo	$a_H = 3.19$ (3.12) Å	$a_H = 3.33$ (3.25) Å	$a_H = 3.56$ (3.47) Å
	$\Delta E = -0.838$ (-0.864) eV	$\Delta E = -0.706$ (-0.709) eV	$\Delta E = -0.515$ (-0.504) eV
W	$a_H = 3.19$ (3.13) Å	$a_H = 3.32$ (3.25) Å	$a_H = 3.56$ (3.48) Å
	$\Delta E = -0.889$ (-0.992) eV	$\Delta E = -0.773$ (-0.773) eV	$\Delta E = -0.565$ (-0.553) eV
Zr	$a_T = 3.69$ (3.61) Å	$a_T = 3.81$ (3.71) Å	$a_T = 3.98$ (3.86) Å
	$\Delta E = 0.543$ (0.525) eV	$\Delta E = 0.417$ (0.412) eV	$\Delta E = 0.288$ (0.312) eV
Hf	$a_T = 3.65$ (3.56) Å	$a_T = 3.77$ (3.57) Å	$a_T = 3.99$ (3.86) Å
	$\Delta E = 0.648$ (0.620) eV	$\Delta E = 0.520$ (0.505) eV	$\Delta E = 0.378$ (0.391) eV

241

242

243 TABLE II. VBM (E_v), CBM (E_c), band gaps (E_g) and work functions (WF) of TMDs calculated by
 244 PBE-SOC. “D” and “I” in the parenthesis after E_g means “direct” and “indirect” band gaps. Due to
 245 the energy level splitting at VBM caused by SOC, the calculated E_g by PBE-SOC is smaller than
 246 that by PBE without SOC.

TMDs	E_v	E_c	E_g (D/I)	WF
MoS ₂	-5.86	-4.27	1.59 (D)	-5.07
MoSe ₂	-5.23	-3.90	1.32 (D)	-4.57
MoTe ₂	-4.76	-3.83	0.94 (D)	-4.29
WS ₂	-5.50	-3.96	1.54 (D)	-4.73
WSe ₂	-4.87	-3.54	1.32 (D)	-4.21
WTe ₂	-4.44	-3.69	0.74 (D)	-4.06
ZrS ₂	-6.79	-5.71	1.08 (I)	-6.25
ZrSe ₂	-6.15	-5.86	0.29 (I)	-6.00
ZrTe ₂	-4.97	-5.69	-0.72 (I)	-4.85
HfS ₂	-6.83	-5.59	1.23 (I)	-6.21
HfSe ₂	-6.17	-5.72	0.45 (I)	-5.94
HfTe ₂	-4.91	-5.53	-0.62 (I)	-4.70

247

248 **Figure Captions**

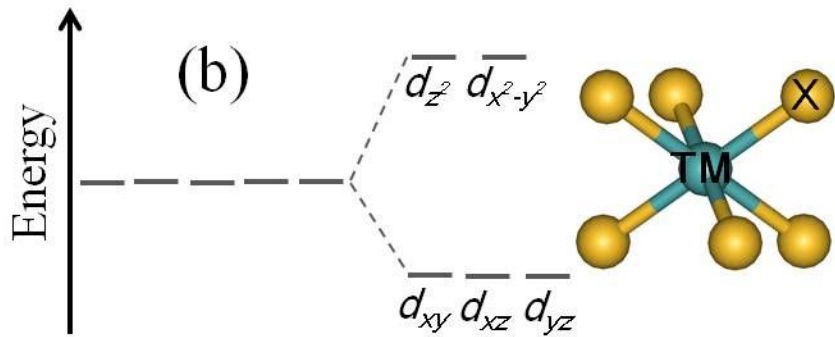
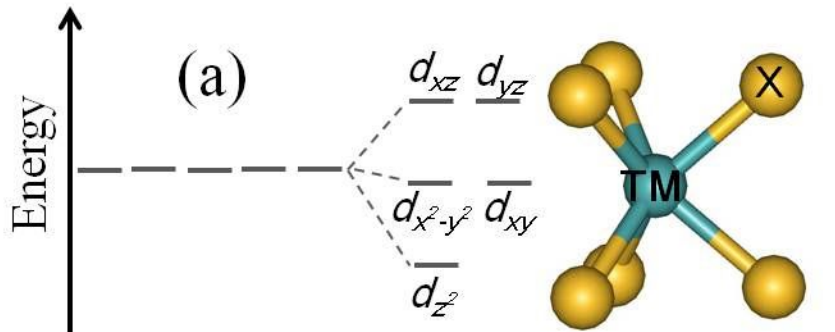
249 FIG. 1. (Color online) The atomic configurations of trigonal prismatic coordination (a) and
250 octahedral coordination (b), and the corresponding *d*-orbitals splittings in trigonal prismatic and
251 octahedral crystal fields. “TM” and “X” in atomic structures represent transition metal atoms and
252 chalcogen atoms.

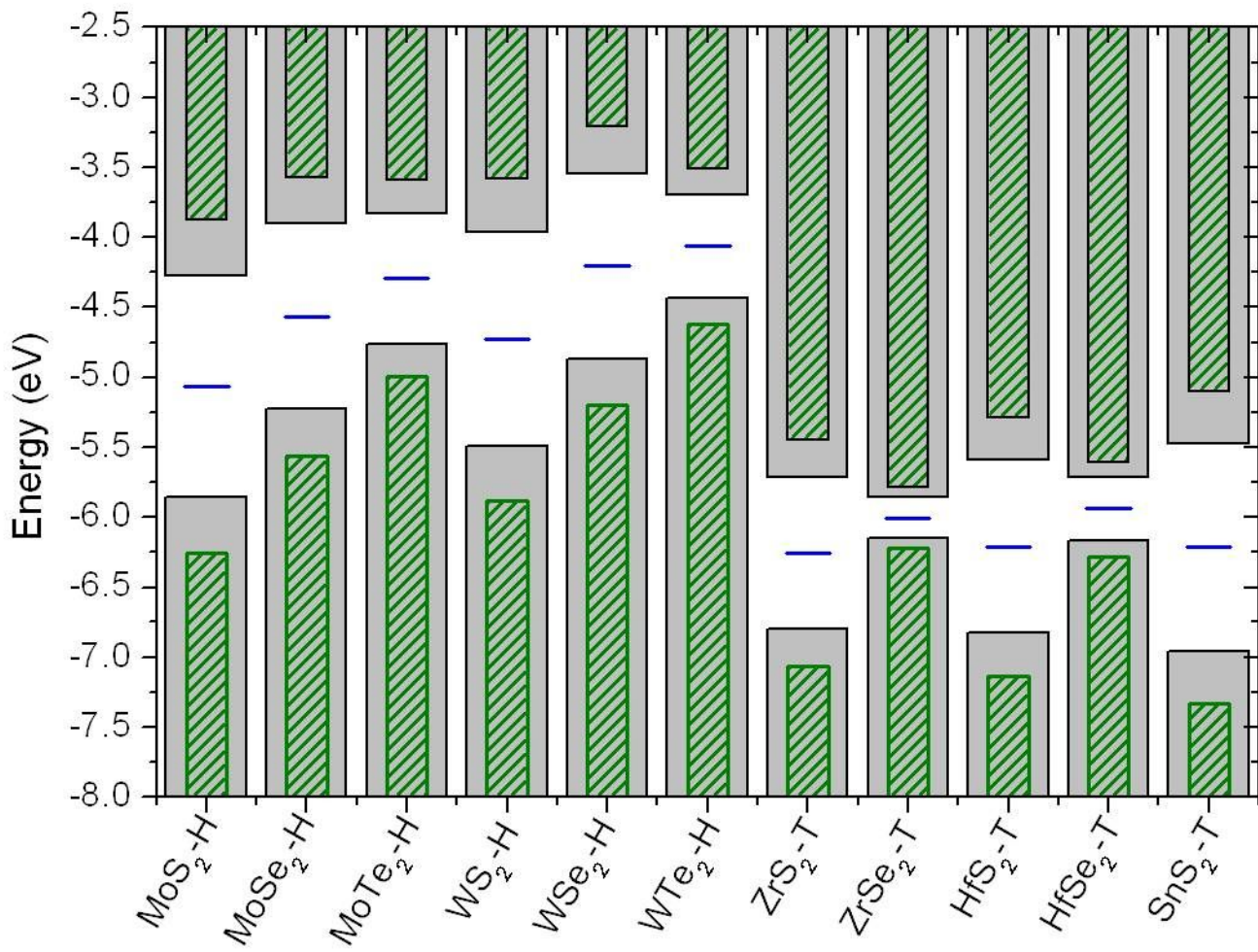
253

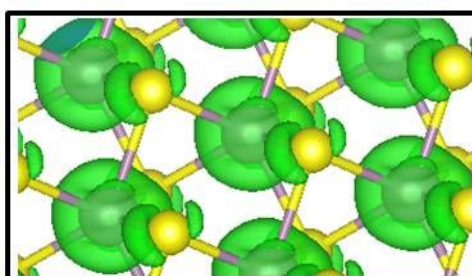
254 FIG. 2. (Color online) Band alignment of monolayer semiconducting TMDs and monolayer SnS₂.
255 CBM and VBM calculated by PBE-SOC are indicated by the filled grey columns, with GW
256 corrected band edges indicated by the narrower olive columns. The Fermi level is indicated by the
257 blue horizontal line and the vacuum level is at 0 eV. SnS₂, as a semiconducting 2D material, is
258 also listed.

259

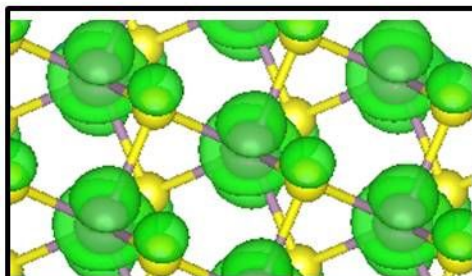
260 FIG. 3. (Color online) Electronic structures of *H*-monolayer MoS₂ (a) and *T*-monolayer ZrS₂ (b)
261 with projected charge distribution at band edges. Yellow, violet and brown balls represent S, Mo,
262 and Zr atoms, respectively. “C” and “V” in parenthesis (for example K(C) and K(V)) mean the
263 conduction band edge and valence band edge at K point





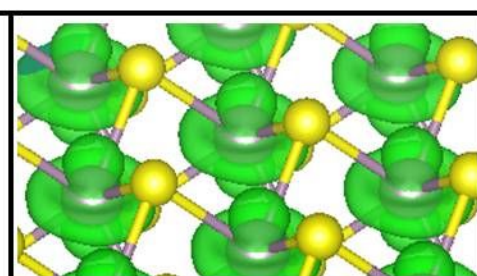
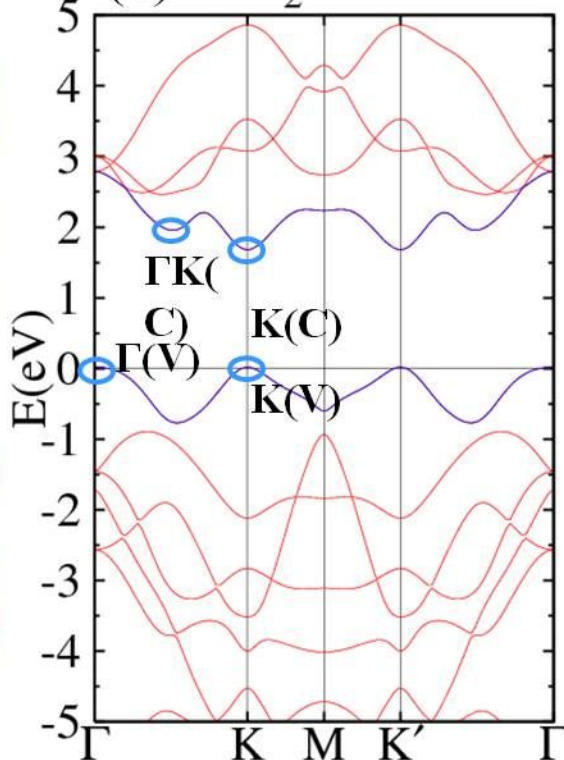


$\Gamma\text{K(C)}$: 30.5%-Mo- d_{z^2} ;
24.8%-Mo- $d(x^2-y^2)$; 24.6%-Mo- d_{xy} ;
6.6%-S- p_x ; 6.6%-S- p_y ; 5.3%-S- p_z .

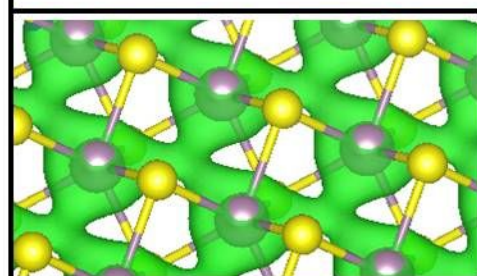


$\Gamma\text{(V)}$: 78.9%-Mo- d_{z^2} ;
19.1%-S- p_z .

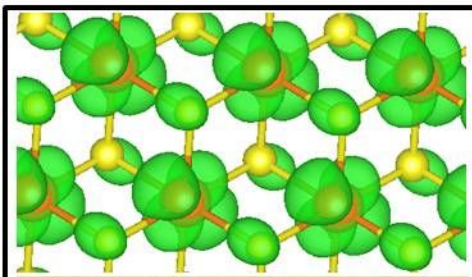
(a) MoS₂-H-PBE



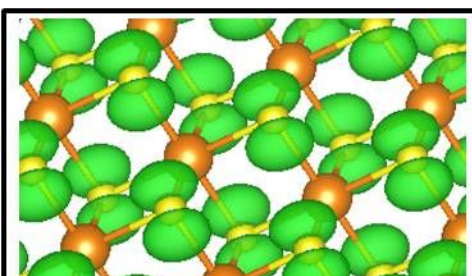
K(C) : 87.7%-Mo- d_{z^2} ;
4.7%-Mo- s ;
4.0%-S- p_x ; 4.1%-S- p_y .



K(V) : 42.1%-Mo- $d(x^2-y^2)$;
41.9%-Mo- d_{xy} ;
7.7%-S- p_x ; 7.7%-S- p_y .

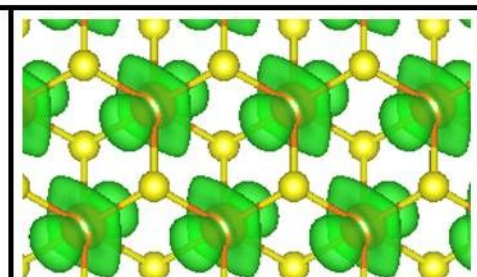
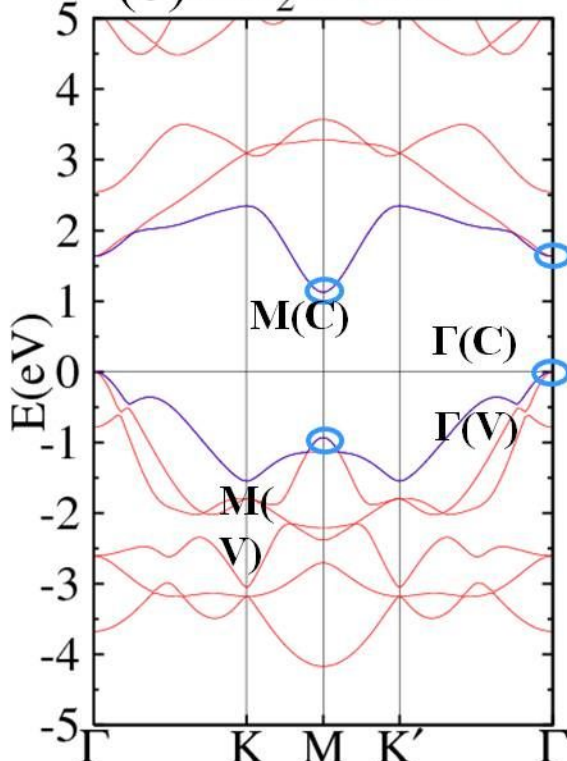


M(C) : 33.9%-Zr- dx_z ; 33.4%-
Zr- dz^2 ; 12.3%-Zr- $d(x^2-y^2)$;
14.3%-S- p_z .

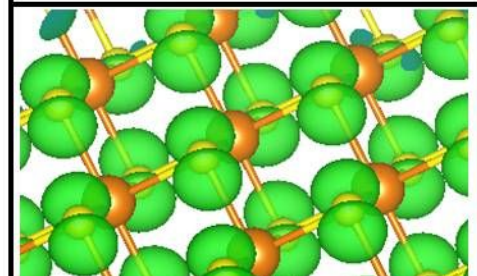


M(V) : 87.3%-S- p_y ;
12.7%-Zr- p_y .

(b) ZrS₂-T-PBE



$\Gamma\text{(C)}$: 66.2%-Zr- dx_z ;
32.4%-Zr- $d(x^2-y^2)$.



$\Gamma\text{(V)}$: 95.4%-S- p_y ;
4.5%-Zr- p_y .